Catalysis Science & Technology

Accepted Manuscript

ROYAL SOCIETY OF CHEMISTRY

www.rsc.org/catalysis

Catalysis Science & Technology RSCPublishing

PAPER

Theoretical Study on the Catalytic Oxidation Mechanism of 5-Hydroxymethylfurfural to 2, 5-Diformylfuran by PMo-Containing Keggin Heteropolyacid

Cite this: DOI: 10.1039/x0xx00000x

Received 00th January 2012,
Accepted 00th January 2012

DOI: 10.1039/x0xx00000x

www.rsc.org/

Li-Ke Ren,[a] Hua-Qing Yang[b*] and Chang-Wei Hu[a *]

The aerobic oxidation mechanism of 5-hydroxymethylfurfural (HMF) to 2,5-diformylfuran (DFF) catalyzed by PMo-containing Keggin heteropolyacid ($H_3PMo_{12}O_{40}$) has been systematically investigated at M06/6-31++G(d, p), Lanl2dz level in dimethylsulfoxide (DMSO). For $H_3PMo_{12}O_{40}$ in DMSO, the most stable species is $[PMo_{12}O_{40}]^{3-}$, which is the catalytic active species for the aerobic oxidation of HMF to DFF. Over $[PMo_{12}O_{40}]^{3-}$ active species, the reaction of 2HMF + O_2 → 2DFF + $2H_2O$ is associated to three successive reaction stages, that is, the oxidation of the first HMF to DFF by $[PMo_{12}O_{40}]^{3-}$, the import of O_2 to form the peroxide $[PMo_{12}O_{41}]^{3-}$, and the oxidation of the second HMF to DFF by $[PMo_{12}O_{41}]^{3-}$, regenerating $[PMo_{12}O_{40}]^{3-}$. The oxidation of each HMF involves two main reaction steps, the cleavage of O-H bond in hydroxyl group and that of C-H bond in methylene group of HMF. The turnover frequency (TOF) determining transition state is the first-step C-H bond cleavage in methylene group of HMF with the rate constant $k_H = 1.345 \times 10^8 \exp(-153{,}476/RT)$, while the TOF determining intermediate is representative of the HMF-containing molecular complex on $[PMo_{12}O_{40}]^{3-}$. The value of kinetic isotope effects (k_H/k_D) is predicted to be 4.2 ~ 5.9, over the 373 ~ 433 K temperature range. The present study brings insight into the catalytically crucial step for the oxidation of HMF to DFF.

1. Introduction

Recently, 5-hydroxymethylfurfural (HMF), as one of the building block platform bridging biomass chemistry and petrochemistry, has been employed as a starting material to produce corresponding derivatives.[1,2] Among them, 2,5-diformylfuran (DFF), as one of the selectively oxidized product of HMF, has been regarded as a potential precursor for the synthesis of pharmaceuticals,[3] fungicides,[4] macrocyclic ligands,[5] and cross-linked agents.[6] Despite its proven usefulness, DFF is commercially available only in milligram quantities and is expensive.

Up to now, the only practical route to DFF is the selective oxidation of HMF, which can be prepared via dehydration of fructose.[7] Selective oxidation of HMF to DFF requires oxidation of its primary hydroxyl group without attacking the more reactive α, β-unsaturated aldehyde group, which would otherwise form 5-hydroxymethyl-2-furancarboxylic acid (HMFCA), 5-formyl-2-furancarboxylic acid (FFCA), and ultimately 2,5-furandicarboxylic acid (FDCA). For this purpose, a number of homogeneous and heterogeneous catalysts, especially those capable of using greener molecular oxygen as oxidant, have been explored. For example, vanadium-containing complexes,[8-14] iron-containing oxides,[15] silver-containing complexes,[16] and ruthenium-containing complexes[17-19] had been found to exhibit good performance. Although the yield of DFF from HMF is very high, the scale synthesis of DFF in applying pure HMF as raw feedstock is limited, due to the energy intensive production and the unstable character of HMF in the purification step, which makes DFF at a prohibitive cost.

Unlike HMF, DFF is a low-polar, hydrophobic compound which can be easily isolated from the reaction solutions due to its insolubility in water and good solubility in many organic solvent. To reduce the cost of DFF, an alternative approach is the direct synthesis of DFF from readily available carbohydrates, without separating the unstable HMF intermediate from solution.[20] For example, Takagaki et al. reported a three-step conversion of glucose to DFF, via the isomerization of glucose to fructose over hydrotalcite (HT), the dehydration of fructose to HMF over Amberlyst-15, and the oxidation of HMF to DFF over Ru/HT catalysts in N,N-dimethylformamide (DMF).[21] Previously, we demonstrated a two-step conversion of glucose to DFF, via the simultaneous isomerization/dehydration of glucose to HMF over $CrCl_3$/NaBr co-catalysts and the oxidation of HMF to DFF over $NaVO_3$ catalyst in DMF.[22] Fu et al. suggested a two-step conversion of fructose to DFF using successive Fe_3O_4-SBA-SO_3H and K-OMS-2 as solid catalysts in dimethylsulfoxide (DMSO).[23]

Recently, we realized the direct conversion of fructose to DFF over Mo-containing Keggin heteropolyacids (HPAs) under air in DMSO, with inference of the dehydration of fructose to HMF over the Brønsted-acid site of HPA and the oxidation of HMF to DFF over the redox site of HPA.[24] Lately, Ghezali et al. demonstrated the direct conversion of fructose and inulin to DFF over Mo-V containing Keggin HPAs in choline chloride/DMSO.[25] Note that all attempts to conduct this reaction in a one-pot process suffer from low activity or difficulty in separation from the reaction solutions, mostly due to the dominant production of humin and other side products. Therefore, more efficient and recyclable catalysts and solvents need to be developed.

To improve the catalytic reactivity for the conversion of carbohydrate to DFF over catalysts in solvents, one can expect to unravel the catalytic mechanism. So far, only limited study[19] has focused on the catalytic mechanism for the conversion of HMF to DFF over Ru/C catalyst. Kinetic isotopic studies showed $k_{C\text{-}H}/k_{C\text{-}D}$=3.73 for the C-H bond cleavage in methylene group and $k_{O\text{-}H}/k_{O\text{-}D}$=1.09 for the O-H bond cleavage in hydroxyl group of HMF molecules.[19] That is to say, the rate-determining step should be the cleavage of C-H bond in methylene group but not that of O-H bond in hydroxyl group of HMF.[19] It is well known that HPAs and their salts possess strong Brønsted acidity and oxidative degradation capacity in solutions, which have been employed for the dehydration of fructose[26,27] or degradation of cellulose[28-30] into platform molecules with the help of its Brønsted acidity, for the transformation of hydrocarbons by the aid of its oxidizability,[31-33] and for the conversion of carbohydrates by means of its bifunctional characteristics.[24,25,34-36] Typically, we have suggested that the Brønsted acidity and redox potential of the HPAs favor the dehydration of fructose and successive oxidation of HMF to DFF, respectively.[24] With regard to the role of Brønsted acidity on the dehydration of fructose to HMF, Assary et al. have obtained the detailed mechanism at the Gaussian-4 level of theory, and suggested that the transformation in acidic media proceed via a much more complex mechanism involving dehydration and hydrogen transfer steps, which are more favourable when proton intermediates are involved.[37] However, the catalytic mechanism underlying the aerobic oxidation of HMF to DFF over HPAs is still not well understood.

In this work, we report the catalytic mechanism for the aerobic oxidation of HMF to DFF over HPA $H_3PMo_{12}O_{40}$ in DMSO. The goals are as follows: (a) to elucidate the existing form of $H_3PMo_{12}O_{40}$ in solution, (b) to provide reliable structures and vibration frequencies of the reactants, intermediates (IMs), transition states (TSs), and products as well as their chemically accurate energetics, (c) to gain a deep insight into the determining transition state (TDTS) and the determining intermediate (TDI) of the turnover frequency (TOF), and (d) to obtain the corresponding kinetics for the aerobic oxidation of HMF to DFF over $H_3PMo_{12}O_{40}$ catalyst.

2. Computational details

All calculations were carried out with the Gaussian 09 program package.[38] Geometry optimizations were run to locate all the stationary points and transition states (TSs), using M06[39] density functional theory method with the 6-31++G(d, p) basis set for hydrogen, carbon, oxygen, and phosphorus,[40-42] and the Lanl2dz basis set and the corresponding effective core potential (ECP) for molybdenum,[43] namely M06/6-31++G(d, p), Lanl2dz. First, for the HPA and its anions, $H_3PMo_{12}O_{40}$, $[H_2PMo_{12}O_{40}]^-$, $[HPMo_{12}O_{40}]^{2-}$, and $[PMo_{12}O_{40}]^{3-}$, full geometry optimizations were performed in the gas phase at M06/6-31++G(d, p), Lanl2dz level. The Conductor-like Screening Model (COSMO) model[44,45] was utilized to simulate the solvent effect of DMSO, via a hybrid M06 functional method[39] with the same basis sets as mentioned above, by partial geometry optimizations based on the optimized structures at M06/6-31++G(d, p), Lanl2dz level in the gas phase. That is to say, the partial geometry optimizations were run in DMSO at M06/6-31++G(d, p), Lanl2dz level, in which the active site involving atoms including Mo atom, its peripheral five O atoms, and H atoms were relaxed, and the remainder atoms were frozen. Next, in the sequential reaction of $[PMo_{12}O_{40}]^{3-}$ + HMF + O_2, partial geometry optimization were performed in DMSO at M06/6-31++G(d, p), Lanl2dz level. That is, for $[PMo_{12}O_{40}]^{3-}$, the active site atoms of $[PMo_{12}O_{40}]^{3-}$ were relaxed together with the substrate molecules, while the remainder atoms of $[PMo_{12}O_{40}]^{3-}$ were frozen on the optimized geometry at M06/6-31++G(d, p), Lanl2dz level. In the meantime, the stability of the wavefunction of the auxiliary Kohn-Sham determinant in density function theory (DFT) was tested.[46,47] If an instability is found, the wavefunction is reoptimized with appropriate reduction in constraints, and the stability tests and reoptimizations are repeated until a stable wavefunction is found.[46,47] Computed $\langle S^2 \rangle$ values suggested that only small spin contamination is included in the calculations. Systematic frequency calculations were performed to characterize stationary points obtained and to take corrections of zero-point energy (ZPE) into account. For the reaction pathway analysis, every transition structure has only one imaginary frequency, and the connections between transition states and corresponding intermediates were verified by means of intrinsic reaction coordinate (IRC) calculations.[48,49] The dominant occupancies of natural bond orbitals and dominant stabilization energies $E(2)$ between donors and acceptors for the typical species have been analyzed with the help of the natural bond orbital (NBO) analysis.[50,51] The critical point charge density ρ was analyzed by the Multiwfn method.[52-54] Unless otherwise mentioned, the Gibbs free energy of formation (ΔG) is relative to the initial ground state reactants including ZPE correction obtained at M06/6-31++G(d, p), Lanl2dz level in DMSO under atmospheric pressure and experimental temperature (1 atm and 433 K).[24]

The turnover frequency (TOF) of the catalytic cycle determines the efficiency of the catalyst. Based on the transition state theory,[55,56] TOF can be calculated by Eqs. (i) and (ii),[57-59] in which δE (the energetic span[60]) is defined as the energy difference between the summit and trough of the catalytic cycle.

$$\mathrm{TOF} = \frac{k_B T}{h} e^{-\frac{\delta E}{RT}} \quad \text{(i)}$$

$$\delta E = \begin{pmatrix} G_{\mathrm{TDTS}} - G_{\mathrm{TDI}} & \text{if TDTS appears after TDI} \\ G_{\mathrm{TDTS}} - G_{\mathrm{TDI}} + \Delta G_r & \text{if TDTS appears before TDI} \end{pmatrix} \quad \text{(ii)}$$

where k_B is the Boltzmann constant, T is the absolute temperature, and h is the Planck constant. G_{TDTS} and G_{TDI} are the Gibbs free energies of the TOF determining transition state (TDTS) and the TOF determining intermediate (TDI), and ΔG_r is the global free energy of the whole cycle.

The rate constants $k(T)$ have been evaluated according to conventional transition state theory (TST) $k`(T)$, including tunneling correction κ(T) based on Wigner's formulation as follows[56]:

$$k^{'}(T) = \frac{k_B T}{hc^0} e^{\frac{-\Delta G^{\neq}}{k_B T}} \quad \text{(iii)}$$

$$\kappa(T) = 1 + \frac{1}{24}\left|\frac{h\omega^{\neq}}{k_B T}\right|^2 \quad \text{(iv)}$$

$$k(T) = \kappa(T) k^{'}(T) \quad \text{(v)}$$

where k_B is the Boltzmann constant, T is the absolute temperature, h is the Planck constant, c^0 is the standard concentration (1 mol dm^{-3}), $\Delta G^{\neq}$ is the activation Gibbs free energy barrier, and $\omega^{\neq}$ is the imaginary frequency of TS.

3. Results and Discussion

The typical HPA anion, $[PMo_{12}O_{40}]^{3-}$, takes on the primary Keggin unit including one PO_4^{3-} anion and one neutral $Mo_{12}O_{36}$ metal-oxygen cage with the symmetry of T_d. Herein, the forty oxygen atoms can be divided into three kinds: four oxygen atoms connecting to P atom, which could be defined as the inner oxygen atoms (O_i); twenty-four oxygen atoms connecting to two Mo atoms, which could be defined as the bridged oxygen atoms (O_b), and the remaining twelve oxygen atoms connecting to one Mo atom by a double bond, which could be defined as the terminal oxygen atoms (O_t). For $H_3PMo_{12}O_{40}$, the geometric structure was fully optimized at M06/6-31++G(d, p), Lanl2dz level, and then compared with the experimental data. Table 1 lists the calculated geometric parameters of $H_3PMo_{12}O_{40}$ in the gas phase together with the experimental data.[61]

Table 1 The calculated geometric parameters (distance in Å and angle in degree) of $H_3PMo_{12}O_{40}$ at the M06/6-31++G(d, p), Lanl2dz level.

Distance/Angle	Calculated value (Å/degree)	Experimental value[a] (Å/degree)
P–O_i	1.55	1.54
Mo–O_i	2.48	2.43 or 2.44
Mo–O_b	1.95	1.91 or 1.92
Mo–O_t	1.67	1.68
O_i–P–O_i	109.5	109.5 or 109.4
O_b–Mo–O_b	87.4	86~89
O_b–Mo–O_t	101.8	101~103

Note: [a]The experimental data are from the Reference [61].

As shown in Table 1, for $H_3PMo_{12}O_{40}$, both the distances of P-O_i, Mo-O_i, Mo-O_b, and Mo–O_t and the angles of O_i-P-O_i, O_b-Mo-O_b, and O_b-Mo-O_t are in good agreement with the experimental data.[61] It is indicated that the present calculation method and basis sets (M06/6-31++G(d, p), Lanl2dz) should be appropriate for the present HPA system.

In the present work, we will mainly discuss the following aerobic oxidation of HMF to DFF over $H_3PMo_{12}O_{40}$ catalyst.

$$2HMF + O_2 \rightarrow 2DFF + 2H_2O \quad (1)$$

For this purpose, we will first discuss the stable structure of $H_3PMo_{12}O_{40}$. According to literatures, the Keggin cluster of heteropolyacid is stable under the temperature of 523 K.[62,63] One can expect that the Keggin cluster of $H_3PMo_{12}O_{40}$ should be stable at 433 K.[24]

Next, we will first discuss the stable species of $H_3PMo_{12}O_{40}$ in DMSO accompanied by water, which originates from the crystallization water of $H_3PMo_{12}O_{40}$.[61] Then we will investigate the following three reactions.

$$[PMo_{12}O_{40}]^{3-} + HMF \rightarrow [H_2PMo_{12}O_{40}]_a^{-} + DFF \quad (2)$$

$$[H_2PMo_{12}O_{40}]_a^{-} + O_2 \rightarrow [PMo_{12}O_{41}]^{3-} + H_2O \quad (3)$$

$$[PMo_{12}O_{41}]^{3-} + HMF \rightarrow [PMo_{12}O_{40}]^{3-} + DFF + H_2O \quad (4)$$

For $[H_{3-x}PMo_{12}O_{40}]^{x-}$ (x = 0~3) species, all the acidic protons are deposited on the O_b site, denoted $H_3PMo_{12}O_{40}$, $[H_2PMo_{12}O_{40}]^{-}$, and $[HPMo_{12}O_{40}]^{2-}$, respectively. Two acidic protons are located on the O_b and on O_t, respectively, denoted as $[H_2PMo_{12}O_{40}]_a^{-}$. Achieving the reaction (1) of 2HMF + O_2 → 2DFF + 2H_2O, the catalytic cycle is composed of (2), (3), and (4) reaction stages. The ΔG_r value of reaction (1) is calculated to be –471.2 kJ mol^{-1}. It is indicated that the reaction (1) in DMSO is thermodynamically favourable. Thereupon, we will discuss the kinetics of the above reactions, vide infra.

Since the ground state of O_2 molecule is the triplet state with the singlet state as the first excited state, particular attention was devoted to the possible occurrence of a two-state reactivity phenomenon. Thus, the potential energy profiles for the ground and the first excited states in the presence of O_2 are investigated. The superscript prefixes "^{1}" and "^{3}" will be used to indicate the singlet and triplet states, respectively. Unless otherwise mentioned, the default state is referred to the ground singlet state.

3.1 Stable species of $H_3PMo_{12}O_{40}$ in solution

Water molecule should be present even in DMSO solvent, which stems from the crystallization water of $H_3PMo_{12}O_{40}$.[61] Both DMSO and water molecules react readily with the Brønsted-acid proton of $H_3PMo_{12}O_{40}$. That is to say, for the capture of proton H^+ from $H_3PMo_{12}O_{40}$, DMSO and H_2O are competitive. To gain insight into the stable species of $H_3PMo_{12}O_{40}$ in DMSO with water, the Gibbs free energy of formation (ΔG) of each species $[H_{3-x}PMo_{12}O_{40}]^{x-}$ starting from independent species ($H_3PMo_{12}O_{40}$ + H_2O or $H_3PMo_{12}O_{40}$ + DMSO) was computed following the reaction

$$H_3PMo_{12}O_{40} + xH_2O \rightarrow [H_{3-x}PMo_{12}O_{40}]^{x-} + xH_3O^+ \quad (5)$$

$$H_3PMo_{12}O_{40} + x\text{DMSO} \rightarrow [H_{3-x}PMo_{12}O_{40}]^{x-} + x\text{DMSOH}^+ \quad (6)$$

and using the equations[64]

$$G_s = G_s^0 + RT\ln\frac{C}{C^0} \quad \text{(vi)}$$

$$\Delta G = G_{[H_{3-x}PMo_{12}O_{40}]^{x-}} + xG_{H_3O^+} - G_{H_3PMo_{12}O_{40}} - xG_{H_2O} \quad \text{(vii)}$$

$$\Delta G = G_{[H_{3-x}PMo_{12}O_{40}]^{x-}} + xG_{DMSOH^+} - G_{H_3PMo_{12}O_{40}} - xG_{DMSO} \quad \text{(viii)}$$

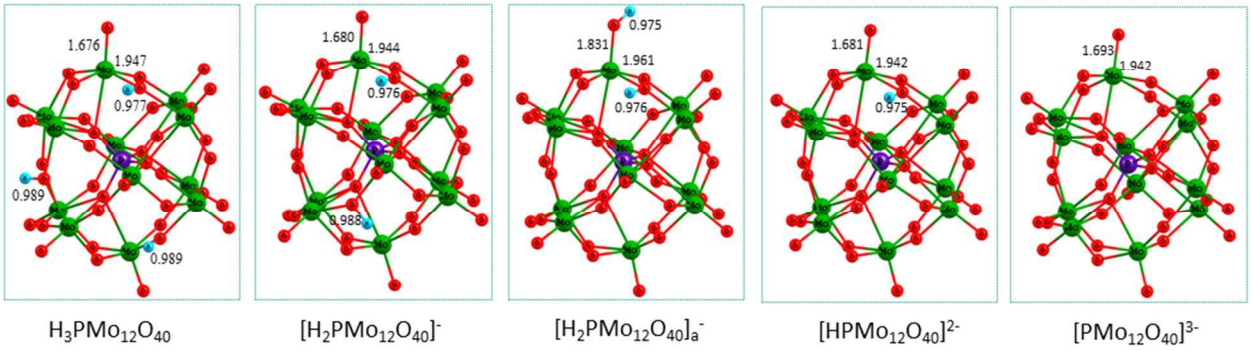

Fig. 1 The geometric structures for the species of $H_3PMo_{12}O_{40}$, $[H_2PMo_{12}O_{40}]^-$, $[H_2PMo_{12}O_{40}]_a^-$, $[HPMo_{12}O_{40}]^{2-}$, and $[PMo_{12}O_{40}]^{3-}$ in DMSO solution. Bond lengths are reported in Å.

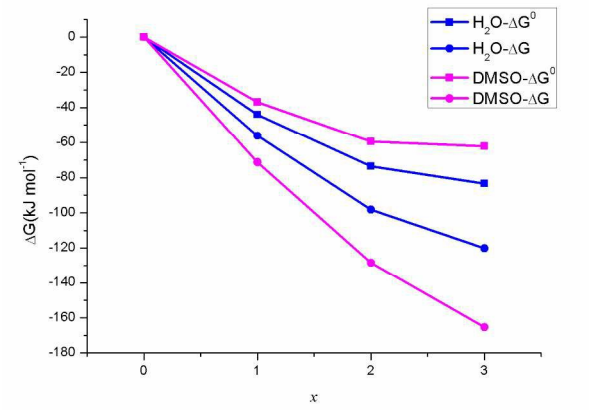

Fig. 2 The Gibbs free energy of formation (ΔG and$\Delta G0$, kJ mol^{-1}) in DMSO as a function of the number of water (x) relative to the $H_3PMo_{12}O_{40}$ + 3H_2O. Blue and pink lines represent the water and DMSO molecules, respectively

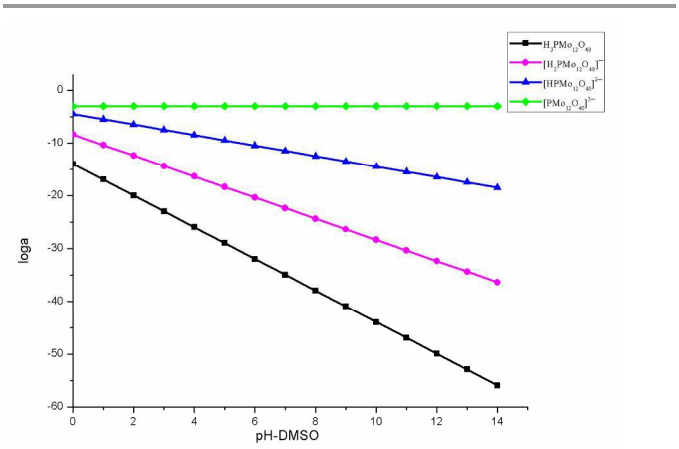

Fig. 3 The common logarithm of mole fraction of the species $[H_{3-x}PMo_{12}O_{40}]^{x-}$ (x = 0~3) in DMSO as a function of solution pH-DMSO.

where R is the universal gas constant, T is the absolute temperature, c^0 is the standard concentration (1 mol dm^{-3}), G_s^0 is the standard Gibbs free energy of species, and G_s is the practical Gibbs free energy of species. The ΔG^0 and ΔG are denoted as the Gibbs free energies of formation for the standard molar concentration of each species (c^0 = 1.0 mol dm^{-3}) and for the practical molar concentration ([$H_3PMo_{12}O_{40}$] = 0.001 mol dm^{-3}, [H_2O] = 0.030 mol dm^{-3}, and [DMSO] = 14.1 mol dm^{-3}) of species, respectively, based on the experimental condition.[24,61]

The geometric structures for the possible species of $H_3PMo_{12}O_{40}$ in DMSO solution with H_2O are shown in Fig. 1. The Gibbs free energies of formation (ΔG^0 and ΔG) in DMSO solution as a function of the number of water (x) relative to the $H_3PMo_{12}O_{40}$ + xH_2O or $H_3PMo_{12}O_{40}$ + DMSO are depicted in Fig. 2.

For $H_3PMo_{12}O_{40}$, NBO analysis shows that the occupancies of Mo–O_t, Mo–O_b, and O_b-H are about 5.82, 1.91, and 1.93 e, respectively, indicating a triplet-bond in Mo–O_t, and a singlet-bond in Mo–O_b and in O_b-H.

As shown in Fig. 2, for $[H_{3-x}PMo_{12}O_{40}]^{x-}$ (x = 0~3) species, both the ΔG^0 and ΔG markedly decreases with increasing number of acidic proton both in the presence of H_2O and DMSO. It is obvious that the $[PMo_{12}O_{40}]^{3-}$ species is the most stable among the four $[H_{3-x}PMo_{12}O_{40}]^{x-}$ (x = 0~3) species in DMSO accompanied by small amount of water. As shown in Fig. 2, for the standard molar concentration of each species, the curve of H_2O locates below that of DMSO. That is to say,

Catalysis Science & Technology RSCPublishing

PAPER

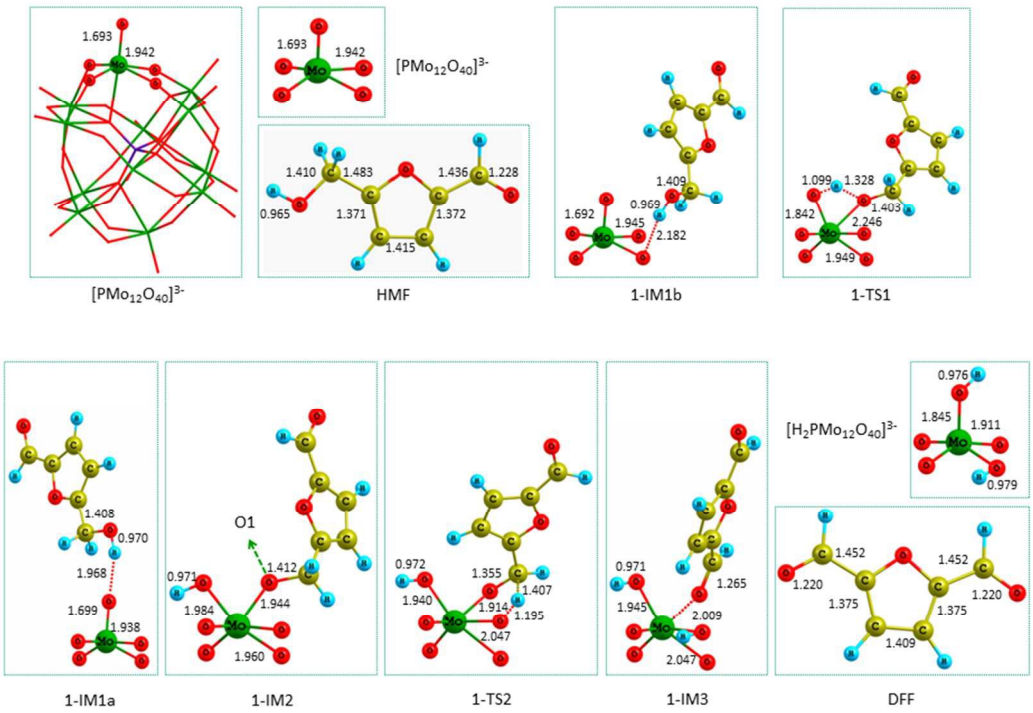

Fig. 4 The geometric structures of species for the reaction of $[PMo_{12}O_{40}]^{3-}$ + HMF → $[H_2PMo_{12}O_{40}]^{3-}$ + DFF. Bond lengths are reported in Å. For concision, only the relaxed atoms near active sites were depicted, whereas the fixed atoms far from the active sites were not depicted.

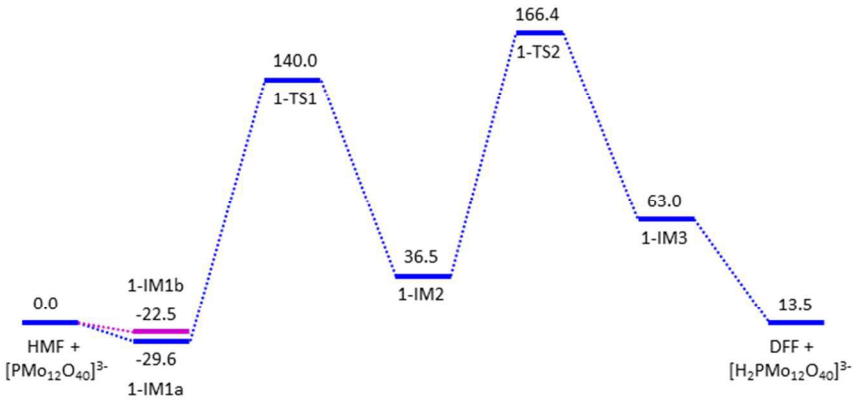

Fig. 5 The schematic energy diagrams for the reaction of $[PMo_{12}O_{40}]^{3-}$ + HMF → $[H_2PMo_{12}O_{40}]^{3-}$ + DFF. Relative energies (kJ mol^{-1}) for the corresponding species plus HMF + O_2 relative to the reactants $[PMo_{12}O_{40}]^{3-}$ + 2HMF + O_2 are shown.

compared with DMSO, H_2O acts as the stronger capture towards proton H^+, when the concentration of H_2O is equal to that of DMSO. On the other hand, for the practical molar concentration of species, the curve of DMSO lies below that of H_2O. It is indicated that the proton H^+ from $H_3PMo_{12}O_{40}$ tends to locate on DMSO, but not on water, because the concentration of DMSO is far larger than that of water in the solution. In other words, compared with H_2O, DMSO behaves as the stronger capture towards proton H^+ in DMSO solution.

In fact, $[H_2PMo_{12}O_{40}]_a^-$ and $[H_2PMo_{12}O_{40}]^-$ are isomers, while $[H_2PMo_{12}O_{40}]_a^-$ lie 12.9 kJ mol^{-1} above $[H_2PMo_{12}O_{40}]^-$. This echoes that the location of the acidic proton is preferred on O_b and not on O_t.[65]

Furthermore, the solution concentration [$DMSOH^+$] of $DMSOH^+$ may have an effect on the stability of $[H_{3-x}PMo_{12}O_{40}]^{x-}$ (x = 0~3) species. Here, the negative of the common logarithm of concentration for $DMSOH^+$ species is defined as the pH-DMSO, and the mole fraction (α) of $[H_{3-x}PMo_{12}O_{40}]^{x-}$ (x = 0~3) species is the ratio of the concentration of $[H_{3-x}PMo_{12}O_{40}]^{x-}$ (x = 0~3) species relative to the concentration of initial $H_3PMo_{12}O_{40}$ (0.001 mol dm^{-3}). Based on this issue, the equilibrium constants (K_x) and the concentration of species for the hydrolysis reaction (6) are computed using the following equations[66-68]

$$K_x = e^{\frac{-\Delta G^0}{RT}} = \frac{\left[H_{3-x}PMo_{12}O_{40}^{x-}\right]\times[DMSOH^+]^x}{\left[H_3PMo_{12}O_{40}\right]\times[DMSO]^x} \quad \text{(ix)}$$

$$\left[H_{3-x}PMo_{12}O_{40}^{x-}\right] = \frac{K_x\times\left[H_3PMo_{12}O_{40}\right]\times[DMSO]^x}{[DMSOH^+]^x} \quad \text{(x)}$$

$$\left[H_3PMo_{12}O_{40}\right] = \frac{[Mo]}{1+\sum_{n=1}^{3}\frac{K_x\cdot[DMSO]^x}{[DMSOH^+]^x}} \quad \text{(xi)}$$

$$\alpha = \frac{\left[H_{3-x}PMo_{12}O_{40}^{x-}\right]}{[Mo]} \quad \text{(xii)}$$

where [Mo] = 0.001 mol dm^{-3} (the initial concentration of $H_3PMo_{12}O_{40}$), [DMSO] = 14.1 mol dm^{-3} (based on the experimental condition).[24] The common logarithm of mole fraction of the $[H_{3-x}PMo_{12}O_{40}]^{x-}$ (x = 0~3) species in DMSO solution as a function of solution pH-DMSO is plotted in Fig. 3.

As shown in Fig. 3, the mole fractions of $[H_{3-x}PMo_{12}O_{40}]^{x-}$ (x = 0~2) species gradually decrease with the increase of pH-DMSO, while the mole fraction of $[PMo_{12}O_{40}]^{3-}$ species is predominated in the 0 ~ 14 pH-DMSO range. It is indicated that the $[PMo_{12}O_{40}]^{3-}$ species is the most stable among the four $[H_{3-x}PMo_{12}O_{40}]^{x-}$ (x = 0 ~ 3) species in DMSO solution. Thereupon, the $[PMo_{12}O_{40}]^{3-}$ species is preferred to the catalytic active species for the aerobic oxidation of HMF to DFF.

3.2 $[PMo_{12}O_{40}]^{3-}$ + HMF → $[H_2PMo_{12}O_{40}]^{3-}$ + DFF

The geometric structures and the schematic energy diagrams for the reaction of (2) $[PMo_{12}O_{40}]^{3-}$ + HMF → $[H_2PMo_{12}O_{40}]^{3-}$ + DFF are depicted in Figs. 4 and 5.

For the HMF molecule, four configurations are investigated both in gas phase and in DMSO solution. For HMF, HMF-2, HMF-3, and HMF-4, the relative Gibbs free energy (G_r) is 0.0, 2.1, 4.6, and 7.2 kJ mol^{-1} in the gas phase, and 0.0, –2.1, 1.9, and –0.3 kJ mol^{-1} in DMSO solution, respectively, as shown in Fig. S1 of Supporting Information (SI). That is to say, in the gas phase, HMF is the most stable. In the DMSO solvent, HMF-2 is the most stable, which locates 2.1 kJ mol^{-1} lower than HMF. However, there are only very few difference in energy among these four configurations of HMF, which fall into the error of the DFT calculation. Furthermore, for HMF and HMF-2, the difference lies only in the position of –CHO group, which keeps invariable in the oxidation reaction from HMF to DFF. Thereupon, HMF, as the most stable in the gas phase, is chosen in the present study.

As shown in Fig. 4, there are four kinds of hydrogen atoms in HMF, which exist on –OH group,–CH_2 group, –CHO group, and furan ring, respectively. From the NBO analysis, the charges of hydrogen atoms are calculated to be +0.54, +0.24, +0.18, and +0.28 on –OH group, –CH_2 group, –CHO group, and furan ring, respectively. As mentioned earlier, there are three kinds of oxygen atoms in $[PMo_{12}O_{40}]^{3-}$, which are the inner oxygen atoms (O_i), the bridged oxygen atoms (O_b), and the terminal oxygen atoms (O_t). By the NBO analysis, the charges of O_i, O_b, and O_t atoms are –1.11, –0.63, and –0.44, respectively. Considering both the steric and charge effects, there are mainly two models of molecular complexes related to the oxidation of HMF to DFF, that is, –OH group of HMF interacting with the O_b and O_t of $[PMo_{12}O_{40}]^{3-}$, respectively.

As shown in Figs. 4 and 5, initially, when HMF molecule interacts with $[PMo_{12}O_{40}]^{3-}$, the hydrogen atom in –OH group of HMF interacts with the O_t and O_b atoms of $[PMo_{12}O_{40}]^{3-}$, respectively, resulting in the molecular complexes 1-IM1a and 1-IM1b, with the stabilization energies of 29.6 and 22.5 kJ mol^{-1}. One can see that 1-IM1a is thermodynamically more preferable than 1-IM1b. For 1-IM1a, the critical point charge density ρ in O_t...H is calculated to be 0.021 e Bohr^{-3}, corresponding to the distances of 1.968 Å. For 1-IM1b, the critical point charge density ρ in O_b...H is calculated to be 0.015 e Bohr^{-3}, corresponding to the distances of 2.182 Å. It is well known that the shorter the distance of the H-bond is, the bigger the critical point charge density ρ in the H-bond is, and the stronger the H-bond is.[52-54] It is obvious that the H-bond in 1-IM1a is stronger than that in 1-IM1b. That is to say, the intermolecular H-bond stabilizes the corresponding complex, in which the steric effect plays a crucial role in the stabilization of the molecular complex. This H-bond effect is similar to methanol and water adsorption on zeolites, in which hydrogen-bonded networks makes the complex stable.[69-71]

Next, from 1-IM1a, a [2+2] addition reaction takes place via a four-membered ring 1-TS1, leading to a hydroxylate 1-IM2 with the energy barrier of 169.6 kJ mol^{-1}. Wherein, the

Catalysis Science & Technology RSCPublishing

PAPER

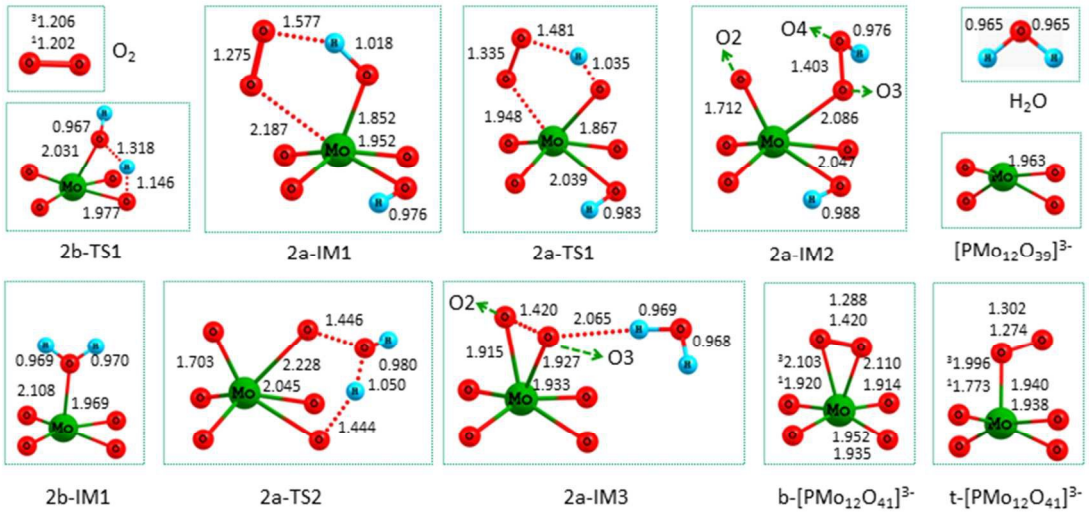

Fig. 6 The geometric structures of species for the reaction of $[H_2PMo_{12}O_{40}]^{3-} + O_2 \rightarrow [PMo_{12}O_{41}]^{3-} + H_2O$. Bond lengths are reported in Å.

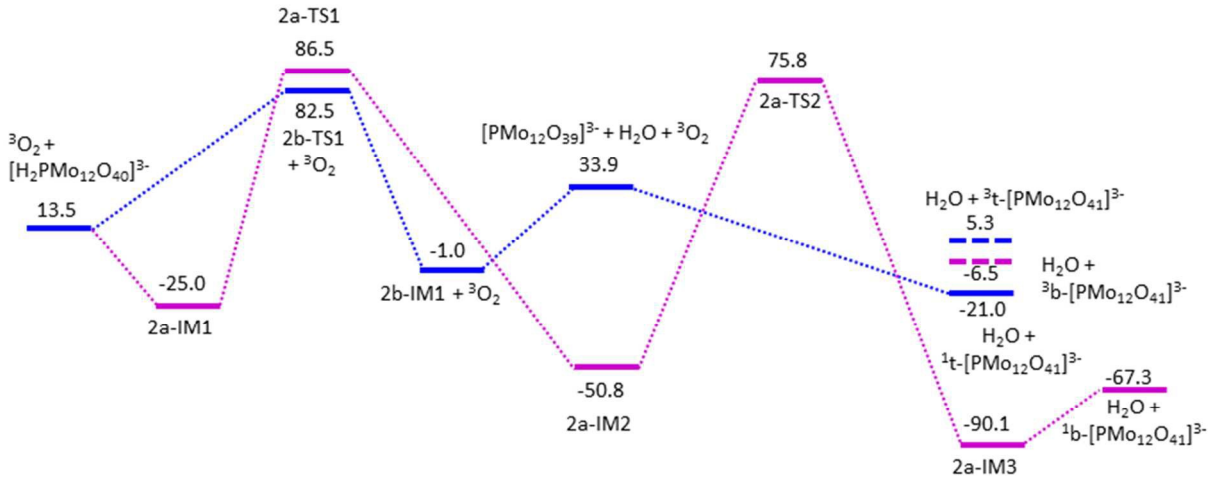

Fig. 7 The schematic energy diagrams for the reaction of $[H_2PMo_{12}O_{40}]^{3-} + O_2 \rightarrow [PMo_{12}O_{41}]^{3-} + H_2O$. Relative energies (kJ mol^{-1}) for the corresponding species plus DFF + H_2O + HMF relative to the reactants $[PMo_{12}O_{40}]^{3-}$ + 2HMF + O_2 are shown.

hydrogen atom in –OH group of HMF migrates to the O_t atom of $[PMo_{12}O_{40}]^{3-}$. For 1-IM2, from NBO analysis, the occupancies of Mo–O_tH and Mo-O1 are 1.929 and 1.940 e, respectively, indicating a complete singlet-bond both in Mo–O_tH and Mo-O1. Then, from the hydroxylate 1-IM2, a [1,4]-H shift occurs with the H atom in $–CH_2$ group migrating to the O_b atom via a five-membered ring 1-TS2, resulting in a DFF-containing molecular complex 1-IM3 with the energy barrier of

129.9 kJ mol^{-1}. For 1-IM3, from the NBO analysis, the occupancies of O_b–H and C-O1 are 1.962 and 3.929 e, respectively, indicating a complete singlet-bond in O_b–H and a complete double-bond in C-O1. It is indicated that HMF has been oxidized to DFF via the shift of the two H atoms in –OH and –CH_2 groups to the O_t and O_b atoms, respectively. Moreover, for 1-IM3, the NBO charges of –DFF and –$H_2PMo_{12}O_{40}$ moiety are +0.19 and -3.19, respectively. Lastly, 1-IM3 set DFF molecule free, leaving $[H_2PMo_{12}O_{40}]^{3-}$ behind. That is to say, HMF is oxidized to DFF while $[PMo_{12}O_{40}]^{3-}$ is reduced to $[H_2PMo_{12}O_{40}]^{3-}$.

From the schematic energy diagrams in Fig. 4, the minimal energy reaction pathway (MERP) involves the energy height of the highest point (EHHP) of 166.4 kJ mol^{-1} at 1-TS2 and the highest energy barrier (HEB) of 169.6 kJ mol^{-1} at the reaction step 1-IM1a → 1-TS1. It is difficult to judge which step is the rate-determining. Therefore, it is necessary to use the energetic span in the whole catalytic cycle.[60]

3.3 $[H_2PMo_{12}O_{40}]^{3-} + O_2 \rightarrow [PMo_{12}O_{41}]^{3-} + H_2O$

The geometric structures and the schematic energy diagrams for the reaction of (3) $[H_2PMo_{12}O_{40}]^{3-} + O_2 \rightarrow [PMo_{12}O_{41}]^{3-} + H_2O$ are depicted in Figs. 6 and 7, respectively. As shown in Figs. 6 and 7, there are two dehydration reaction pathways, which proceed after and before the introduction of O_2, denoted as "**RP-a**" and "**RP-b**", respectively.

As depicted in Figs. 6 and 7, for **RP-a**, for the O_2 molecule, the ground state is the triplet state, with the singlet state as the first excited state at 156.2 kJ mol^{-1} above the ground triplet state. Initially, when O_2 interacts with $[H_2PMo_{12}O_{40}]^{3-}$, a molecular complex 2a-IM1 is formed with the stabilization energies of 20.5 and 38.5 kJ mol^{-1} at the ground triplet and the singlet states, respectively. From 2a-IM1, the hydrogen atom of –OH transfers to the –O_2 moiety with a five-membered ring 2a-TS1, leading to a peroxide hydride 2a-IM2. For the ground singlet 2a-IM2, the occupancies of Mo-O2, Mo-O3, O3-O4, and O4-H are 5.799, 1.971, 1.988, and 1.990 *e*, respectively, indicating an approximate triplet bond in Mo-O2, a complete singlet bond in Mo-O3, O3-O4, and O4-H. From 2a-IM2, a [1,4]-H shift takes place from -O_bH group to O4 via a five-membered ring 2a-TS2, resulting in a water molecular complex 2a-IM3. For the ground singlet 2a-IM3, the occupancies of Mo-O2, Mo-O3, and O2-O3 are 1.885, 1.890, and 1.983 *e*, respectively, indicating a singlet bond in each one. That is to say, a three-member cycle exists in Mo-O2-O3. Lastly, 2a-IM3 set a water molecule free, leaving a bridge b-$[PMo_{12}O_{41}]^{3-}$ behind.

As shown in Figs. 6 and 7, for **RP-b**, from $[H_2PMo_{12}O_{40}]^{3-}$, a [1,3]-H shift takes place from –O_bH to O2 via a four-membered ring 2b-TS1, producing a water molecular complex 2b-IM1. Next, 2b-IM1 liberates the water molecule free, saving $[PMo_{12}O_{39}]^{3-}$ behind. Then, O_2 molecule attacks the Mo site of $[PMo_{12}O_{39}]^{3-}$, through one or two O-end interacting with Mo, yielding a terminal t-$[PMo_{12}O_{41}]^{3-}$ or a bridge b-$[PMo_{12}O_{41}]^{3-}$, respectively. For the terminal t-$[PMo_{12}O_{41}]^{3-}$, the singlet ground state lies 26.3 kJ mol^{-1} below the triplet state. For the bridge b-$[PMo_{12}O_{41}]^{3-}$, the ground singlet state deposits 60.8 kJ mol^{-1} below the triplet state. Moreover, the ground state bridge b-$[PMo_{12}O_{41}]^{3-}$ locates 46.3 kJ mol^{-1} below the ground state terminal t-$[PMo_{12}O_{41}]^{3-}$. It is indicated that the bridge b-$[PMo_{12}O_{41}]^{3-}$ is thermodynamically more stable than the terminal t-$[PMo_{12}O_{41}]^{3-}$. By NBO analysis, for the ground singlet t-$[PMo_{12}O_{41}]^{3-}$, the occupancies of Mo-O2 and O2-O3 are 5.702 and 1.988 *e*, respectively, indicating an approximate triplet bond in Mo-O2 and a complete singlet bond in O2-O3. For the ground singlet b-$[PMo_{12}O_{41}]^{3-}$, the occupancies of Mo-O2, Mo-O3, and O2-O3 are 1.883, 1.889, and 1.982 *e*, respectively, indicating a complete singlet bond in each one. From the singlet bond characteristic and the lengthened distance in O2-O3, one can see that the O_2 molecule has been activated after adsorbing on $[PMo_{12}O_{39}]^{3-}$.

For **RP-a**, the minimal energy reaction pathway (MERP) involves the highest energy barrier (HEB) of 126.6 kJ mol^{-1} at the 2a-IM2 → 2a-TS2 reaction step, and the energy height of the highest point (EHHP) of 86.5 kJ mol^{-1} at 2a-TS1. Alternatively, for **RP-b**, the MERP includes the HEB of 69.0 kJ mol^{-1} at the $[H_2PMo_{12}O_{40}]^{3-}$ → 2b-TS1 reaction step, and the EHHP of 82.5 kJ mol^{-1} at 2b-TS1. It is evident that both the HEB and EHHP for **RP-a** are higher than those for **RP-b**, respectively. Thereupon, the **RP-b** is kinetically more favourable than the **RP-a**.

3.4 $[PMo_{12}O_{41}]^{3-} + HMF \rightarrow [PMo_{12}O_{40}]^{3-} + DFF + H_2O$

The geometric structures and the schematic energy diagrams for the reaction of (4) $[PMo_{12}O_{41}]^{3-} + HMF \rightarrow [PMo_{12}O_{40}]^{3-} + DFF + H_2O$ are depicted in Figs. 8 and 9, respectively.

As mentioned earlier, for $[PMo_{12}O_{41}]^{3-}$, there are two configurations, the bridge b-$[PMo_{12}O_{41}]^{3-}$ and the terminal t-$[PMo_{12}O_{41}]^{3-}$. It is obvious that the Mo active centre is six-coordination and seven-coordination in b-$[PMo_{12}O_{41}]^{3-}$ and t-$[PMo_{12}O_{41}]^{3-}$, respectively. Owning to the steric hindrance, the six-coordinated b-$[PMo_{12}O_{41}]^{3-}$ is more beneficial to react with HMF than the seven-coordinated t-$[PMo_{12}O_{41}]^{3-}$. The bridge b-$[PMo_{12}O_{41}]^{3-}$ can easily isomerize to the terminal t-$[PMo_{12}O_{41}]^{3-}$, with the energy requirement of 46.3 kJ mol^{-1}. In the beginning, the hydrogen atom on –OH group of HMF interacts with the O3 atom of t-$[PMo_{12}O_{41}]^{3-}$ via H-bond, leading to a molecular complex 3-IM1, with the stabilization energy of 21.7 kJ mol^{-1}. For 3-IM1, the critical point charge density ρ in O3...H is calculated to be 0.024 *e* Bohr^{-3}, corresponding to the distances of 1.963 Å. From 3-IM1, a [2+3] addition reaction takes place via a five-membered ring 3-TS1, resulting in a peroxide hydride 3-IM2 with the energy barrier of 132.0 kJ mol^{-1}. For 3-IM2, the occupancies of Mo-O2, Mo-O4, O2-O3, and O3-H are 1.906, 1.915, 1.990, and 1.989 *e*, respectively, indicating a complete singlet bond in each one, by NBO analysis. From 3-IM2, the hydrogen atom on –CH_2 group needs to be oxidized. To arrive at the end, there are two reaction pathways, through the bridge O_b and the terminal O3, respectively, denoted as **RP-Ob** and **RP-Ot**.

On the one hand, for **RP-Ob**, from 3-IM2, [1,4]-H shift occurs via a five-membered ring 3a-TS2, generating a DFF

Catalysis Science & Technology RSCPublishing

PAPER

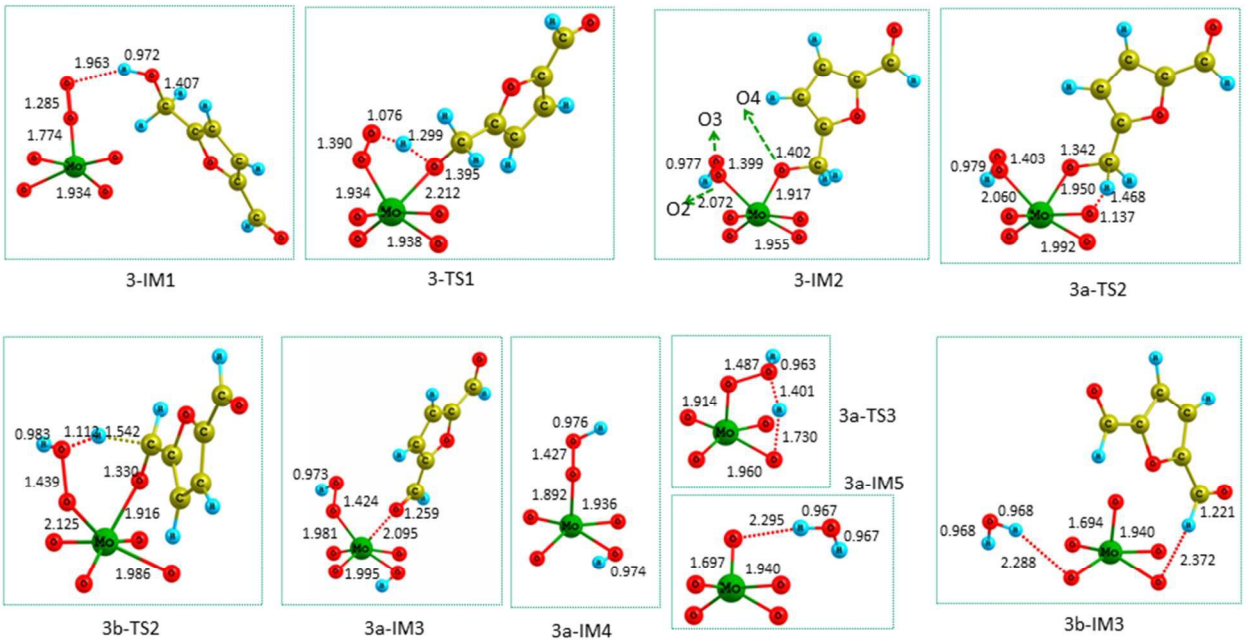

Fig. 8 The geometric structures of species for the reaction of $[PMo_{12}O_{41}]^{3-}$ + HMF → $[PMo_{12}O_{40}]^{3-}$ + DFF + H_2O. Bond lengths are reported in Å.

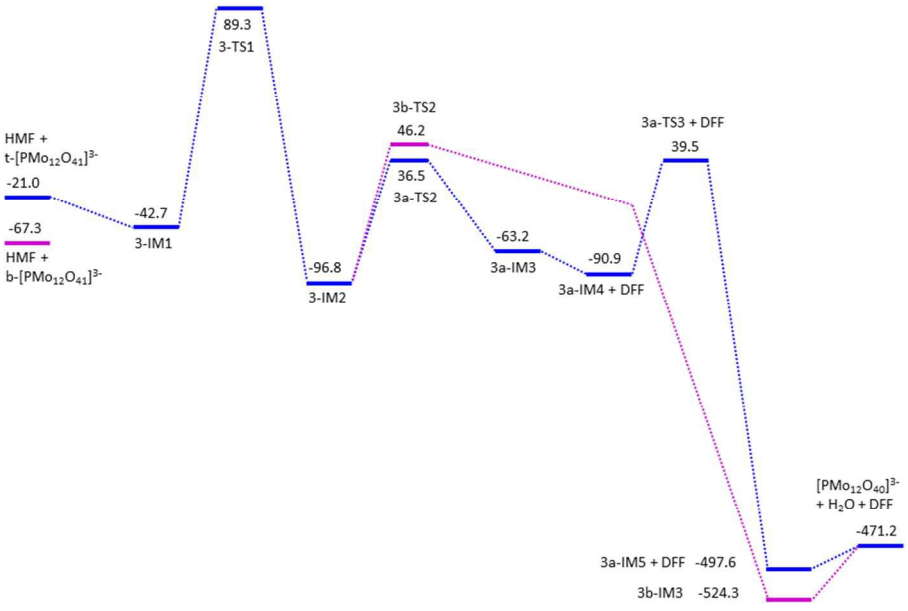

Fig. 9 The schematic energy diagrams for the reaction of $[PMo_{12}O_{41}]^{3-}$ + HMF → $[PMo_{12}O_{40}]^{3-}$ + DFF + H_2O. Relative energies (kJ mol^{-1}) for the corresponding species plus DFF + $2H_2O$ relative to the reactants $[PMo_{12}O_{40}]^{3-}$ + 2HMF + O_2 are shown.

Catalysis Science & Technology RSCPublishing

PAPER

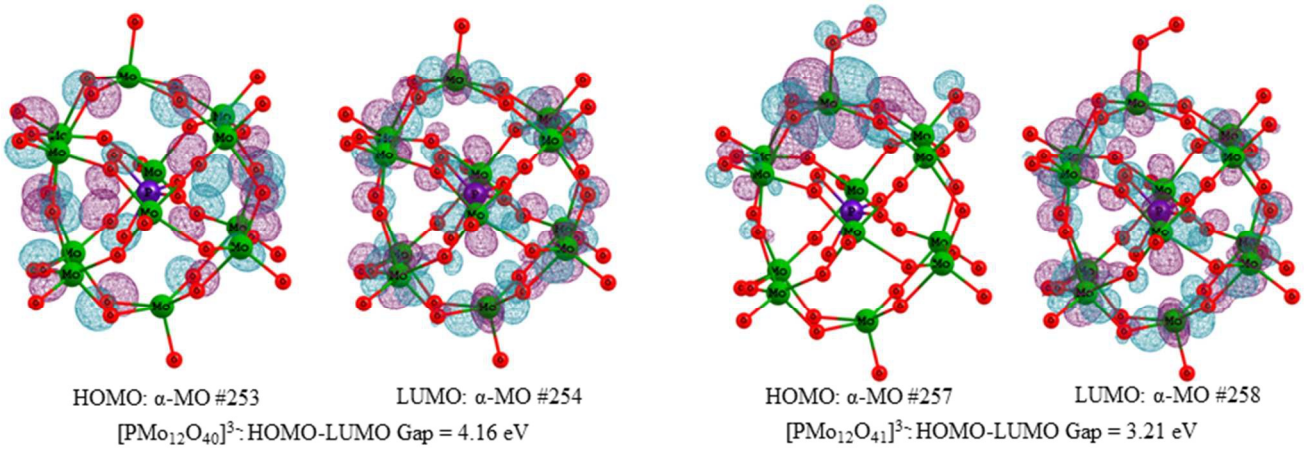

Fig. 10 Highest occupied molecular orbital (HOMO), lowest unoccupied molecular orbital (LUMO), and the HOMO-LUMO energy gap for the $[PMo_{12}O_{40}]^{3-}$ and $[PMo_{12}O_{41}]^{3-}$. The orbital contour value is 0.03.

molecular complex 3a-IM3, with the energy barrier of 133.3 kJ mol^{-1}. After that, 3a-IM3 set the DFF molecule free, leaving 3a-IM4 behind, with the exoergicity of 27.7 $kJmol^{-1}$. Next, from 3a-IM4, a [1,4]-H shift takes place again via a five-membered ring 3a-TS3, yielding a water molecular complex 3a-IM5, with the energy barrier of 130.4 kJ mol^{-1}. Finally, 3a-IM5 liberates the water molecule free, regenerating the catalyst $[PMo_{12}O_{40}]^{3-}$, with endoergicity of 26.4 kJ mol^{-1}. This reaction pathway **RP-Ob** involves the HEB of 133.3 kJ mol^{-1} at the 3-IM3 → 3a-TS2 reaction step and the EHHP of 39.5 kJ mol^{-1} at 3a-TS3.

On the other hand, for **RP-Ot**, from 3-IM2, a [1,5]-H shift tales place via a six-membered ring 3b-TS2, resulting in a water and DFF containing molecular complex 3b-IM3, with the energy barrier of 143.0 kJ mol^{-1}. Then, 3b-IM3 releases the water and DFF molecules free, reviving the catalyst $[PMo_{12}O_{40}]^{3-}$, with endoergicity of 53.1 kJ mol^{-1}. This reaction pathway **RP-Ot** includes the HEB of 143.0 kJ mol^{-1} at the 3-IM3 → 3b-TS2 reaction step and the EHHP of 46.2 kJ mol^{-1} at 3b-TS2.

Comparing with **RP-Ot**, **RP-Ob** is almost kinetically equal, because of its proximate HEB (143.0 *vs* 133.3 kJ mol^{-1}) and lower EHHP (39.5 *vs* 46.2 kJ mol^{-1}).

For the whole catalytic cycle in the MERP, the TDI and TDTS are 1-IM1a and 1-TS2, respectively, by TOF analysis using energetic span model. As mentioned earlier, 1-IM1a is the HMF-containing molecular complex, and 1-TS2 is associated with the C-H bond cleavage in methylene group in the first HMF. It is indicated that the oxidation of the second HMF on the peroxide $[PMo_{12}O_{41}]^{3-}$ proceeds more readily than the oxidation of the first HMF on $[PMo_{12}O_{40}]^{3-}$.

To explain the different reactivity of the two species, $[PMo_{12}O_{40}]^{3-}$ and $[PMo_{12}O_{41}]^{3-}$, the HOMO and LUMO molecular orbitals are depicted in Fig. 10. As shown in Fig. 10, the HOMO-LUMO gaps are 4.16 and 3.21 eV for $[PMo_{12}O_{40}]^{3-}$ and $[PMo_{12}O_{41}]^{3-}$, respectively. It is apparent that the HOMO-LUMO gap for $[PMo_{12}O_{40}]^{3-}$ is larger than that for $[PMo_{12}O_{41}]^{3-}$. It is indicated that $[PMo_{12}O_{40}]^{3-}$ possesses lower reactivity and higher kinetics stability than $[PMo_{12}O_{41}]^{3-}$. Furthermore, for $[PMo_{12}O_{40}]^{3-}$, the HOMO of α-MO #253 involves 0.3% s-orbital and 99.7% p-orbital of oxygen atom contributions, and the LUMO of α-MO #254 includes 0.2% s-orbital, 97.7% p-orbital, and 2.1% d-orbital of molybdenum atom contributions. For $[PMo_{12}O_{41}]^{3-}$, the HOMO of α-MO #257 involves 0.7% s-orbital and 99.2% p-orbital of oxygen atom contributions, and the LUMO of α- MO #258 includes 10.4% s-orbital, 82.5% p-orbital, and 7.2% d-orbital of molybdenum atom contributions. It is indicated that there exists different HOMO-LUMO orbital interactions in $[PMo_{12}O_{40}]^{3-}$ and in $[PMo_{12}O_{41}]^{3-}$, which make them perform differently in the reaction. For the C-H bond cleavage in methylene group in HMF, as the crucial reaction step in the catalytic cycle, the higher oxidizability of the species is responsible for the easier reaction.

In addition, the TOF analysis results indicate that the rate-determining step is the cleavage of C-H bond in methylene group but not that of O-H bond in hydroxyl group of HMF.

This echoes the experimental result for the conversion of HMF to DFF over Ru/C catalyst, in which the rate-determining step is the cleavage of C-H bond in methylene group but not that of O-H bond in hydroxyl group of HMF.[19] Herein, the rate constant k_H of 1-IM1a → 1-TS2 is representative of the whole reaction constant for the gross reaction (1) 2HMF + O_2 → 2DFF + 2H_2O. Over the 373 ~ 433 K temperature range, the rate constant k_H can be fitted by the following expression (in s^{-1}):

$$k_H = 1.345\times10^8 \exp(-153,476/RT) \quad \text{(xii)}$$

Furthermore, to predict the kinetic isotope effects (KIEs), the rate constant k_D of 1-IM1a → 1-TS2 is also evaluated for the deuterium-substituted forms in methylene group of HMF. Over the 373 ~ 433 K temperature range, the rate constant k_D can be fitted by the following expression (in s^{-1}):

$$k_D = 2.741\times10^8 \exp(-161,175/RT) \quad \text{(xiii)}$$

The value of KIEs (k_H/k_D) is calculated to be 5.9 ~ 4.2, over the 373 ~ 433 K temperature range. This result is close to the experimental observation (k_H/k_D = 3.7) for the conversion of HMF to DFF over Ru/C catalyst at 353 K temperature.[19]

Summarily, over $[PMo_{12}O_{40}]^{3-}$ active species, the reaction of 2HMF + O_2 → 2DFF + 2H_2O is associated to three successive reaction stages, the oxidation of the first HMF to DFF over $[PMo_{12}O_{40}]^{3-}$, the import of O_2 to form the peroxide $[PMo_{12}O_{41}]^{3-}$, and the oxidation of the second HMF to DFF by $[PMo_{12}O_{41}]^{3-}$. The oxidation of each HMF involves two main reaction steps, the cleavage of O-H bond in hydroxyl group and that of C-H bond in methylene group of HMF. The TOF determining transition state is characteristic of the cleavage of C-H bond in methylene group of the first HMF, while the TOF determining intermediate is representative of the HMF containing molecular complex on $[PMo_{12}O_{40}]^{3-}$. The peroxide $[PMo_{12}O_{41}]^{3-}$ exhibits higher oxidation performance than $[PMo_{12}O_{40}]^{3-}$ for the oxidation of HMF to DFF.

Furthermore, for the reaction of 2HMF + O_2 → 2DFF + 2H_2O over $[PMo_{12}O_{40}]^{3-}$ active species, it can be seen that the oxygen source originates both from O_2 molecule and from $[PMo_{12}O_{40}]^{3-}$ catalytic species. When $[PMo_{12}O_{40}]^{3-}$ provides one oxygen atom to oxidize the first HMF to DFF, the oxygen-vacancy $[PMo_{12}O_{39}]^{3-}$ is formed, which promotes the indirect dissociation of O_2 molecule by the oxidation of HMF to DFF. This can be ascribed to the fact that the peroxide $[PMo_{12}O_{41}]^{3-}$ exhibits higher oxidation performance than $[PMo_{12}O_{40}]^{3-}$. This result is different from that over Ru catalyst, in which the oxygen source stems only from O_2 molecule and requires the direct dissociation of O_2 molecule on catalytic site.[19]

Conclusions

The aerobic oxidation mechanism of HMF to DFF catalyzed by PMo-containing Keggin heteropolyacid has been theoretically investigated. The following conclusions can be drawn from the present calculation.

For the PMo-containing Keggin heteropolyacid $H_3PMo_{12}O_{40}$ in DMSO accompanied by water, the most stable species is $[PMo_{12}O_{40}]^{3-}$ in the 0 ~ 14 pH range, which is the catalytically active species for the aerobic oxidation of HMF to DFF.

Over $[PMo_{12}O_{40}]^{3-}$ active species, the reaction of 2HMF + O_2 → 2DFF + 2H_2O is associated to three successive reaction stages, the oxidation of the first HMF to DFF by $[PMo_{12}O_{40}]^{3-}$, the import of O_2 to form the peroxide $[PMo_{12}O_{41}]^{3-}$, and the oxidation of the second HMF to DFF by $[PMo_{12}O_{41}]^{3-}$, regenerating $[PMo_{12}O_{40}]^{3-}$. The oxidation of each HMF involves two main reaction steps, the cleavage of O-H bond in hydroxyl group and that of C-H bond in methylene group of HMF.

The turnover frequency (TOF) determining transition state is characteristic of the first-step C-H bond cleavage in methylene group of HMF with the rate constant $k_H = 1.345 \times 10^8 \exp(-153,476/RT)$, while the TOF determining intermediate is representative of the HMF containing molecular complex on $[PMo_{12}O_{40}]^{3-}$. The value of kinetic isotope effects KIEs (k_H/k_D) is predicted to be 5.9 ~ 4.2, over the 373 ~ 433 K temperature range. The peroxide $[PMo_{12}O_{41}]^{3-}$ exhibits better oxidation performance than $[PMo_{12}O_{40}]^{3-}$ for the oxidation of HMF to DFF.

Acknowledgements

The authors are grateful for financial support by the National Natural Science Foundation of China (No: 21573154) and the Applied Foundation Research of Sichuan Province (No: 2014JY0218).

Notes and references

[a] Key Laboratory of Green Chemistry and Technology, Ministry of Education, College of Chemistry, Sichuan University, Chengdu, Sichuan, 610064, P.R. China

[b] College of Chemical Engineering, Sichuan University, Chengdu, Sichuan, 610065, P.R. China

† Electronic Supplementary Information (ESI) available: [Thermal correction to Gibbs free energy (G_0, hartree), sum of electronic and thermal free energies (G_c, hartree), and relative energies (G_r, kJ mol^{-1}) various species with respect to the ground reactants calculated at M06/6-31++G(d, p), Lanl2dz level in dimethysulfoxide (DMSO) under atmospheric pressure and experimental temperature (433 K and 1 atm). The standard orientations of various species calculated at the M06/6-31++G(d, p), Lanl2dz level in the aerobic oxidation of HMF to DFF over the PMo-containing Keggin heteropolyacid $H_3PMo_{12}O_{40}$. Arrhenius plots of calculated rate constants for the crucial reaction step in aerobic oxidation of HMF to DFF over $[PMo_{12}O_{40}]^{3-}$.]. See DOI: 10.1039/b000000x/

1 O. O. James, S. Maity, L. A. Usman, K. O. Ajanaku, O. O. Ajani, T. O. Siyanbola, S. Sahu and R. Chaubey, *Energy. Environ. Sci*., 2010, **3**, 1833-1850.

2 M. M. Antunes, P. A. Russo, P. V. Wiper, J. M. Veiga, M. Pillinger, L. Mafra, D. V. Evtuguin, N. Pinna and A. A. Valente, *Chemsuschem*, 2014, **7**, 804-812.

3 K. T. Hopkins, W. D. Wilson, B. C. Bender, D. R. McCurdy, J. E. Hall, R. R. Tidwell, A. Kumar, M. Bajic and D. W. Boykin, *J. Med. Chem.*, 1998, **41**, 3872-3878.
4 M. Del Poeta, W. A. Schell, C. C. Dykstra, S. Jones, R. R. Tidwell, A. Czarny, M. Bajic, M. Bajic, A. Kumar, D. W. Boykin and J. R. Perfect, *Antimicrob. Agents. Ch.*, 1998, **42**, 2495-2502.
5 D. T. Richter and T. D. Lash, *Tetrahedron Lett.*, 1999, **40**, 6735-6738.
6 D. W. Sheibley, M. A. Manzo and O. D. Gonzalezsanabria, *J. Electro. Soc.*, 1983, **130**, 255-259.
7 F. W. Lichtenthaler, *Acc. Chem. Res.*, 2002, **35**, 728-737.
8 C. Carlini, P. Patrono, A. M. R. Galletti, G. Sbrana and V. Zima, *Appl. Catal. A*, 2005, **289**, 197-204.
9 O. C. Navarro, A. C. Canos and S. I. Chornet, *Top. Catal.*, 2009, **52**, 304-314.
10 J. P. Ma, Z. T. Du, J. Xu, Q. H. Chu and Y. Pang, *Chemsuschem*, 2011, **4**, 51-54.
11 J. F. Nie and H. C. Liu, *Pure. Appl. Chem.*, 2012, **84**, 765-777.
12 I. Sadaba, Y. Y. Gorbanev, S. Kegnaes, S. S. R. Putluru, R. W. Berg and A. Riisager, *Chemcatchem*, 2013, **5**, 284-293.
13 F. L. Grasset, B. Katryniok, S. Paul, V. Nardello-Rataj, M. Pera-Titus, J. M. Clacens, F. De Campo and F. Dumeignil, *RSC Adv.*, 2013, **3**, 9942-9948.
14 N. T. Le, P. Lakshmanan, K. Cho, Y. Han and H. Kim, *Appl. Catal. A*, 2013, **464**, 305-312.
15 B. Liu, Z. H. Zhang, K. L. Lv, K. J. Deng and H. M. Duan, *Appl. Catal. A*, 2014, **472**, 64-71.
16 G. D. Yadav and R. W. Sharma, *Appl. Catal. B*, 2014, **147**, 293-301.
17 C. A. Antonyraj, J. Jeong, B. Kim, S. Shin, S. Kim, K. Y. Lee and J. K. Cho, *J. Ind. Eng. Chem.*, 2013, **19**, 1056-1059.
18 Y. M. Wang, B. Liu, K. C. Huang and Z. H. Zhang, *Ind. Eng. Chem. Res.*, 2014, **53**, 1313-1319.
19 J. F. Nie, J. H. Xie and H. C. Liu, *J. Catal.*, 2013, **301**, 83-91.
20 G. A. Halliday, R. J. Young and V. V. Grushin, *Org. Lett.*, 2003, **5**, 2003-2005.
21 A. Takagaki, M. Takahashi, S. Nishimura and K. Ebitani, *ACS Catal.*, 2011, **1**, 1562-1565.
22 X. Xiang, L. He, Y. Yang, B. Guo, D. M. Tong and C. W. Hu, *Catal. Lett.*, 2011, **141**, 735-741.
23 Z. Z. Yang, J. Deng, T. Pan, Q. X. Guo and Y. Fu, *Green Chem.*, 2012, **14**, 2986-2989.
24 Y. Liu, L. F. Zhu, J. Q. Tang, M. Y. Liu, R. D. Cheng and C. W. Hu, *Chemsuschem*, 2014, **7**, 3541-3547.
25 W. Ghezali, V. K. De Oliveira, R. Kessas and F. Jerome, *Green Chem.*, 2015, **17**, 4459-4464.
26 K.-i. Shimizu, R. Uozumi and A. Satsuma, *Catal. Commun.*, 2009, **10**, 1849-1853.
27 Q. Zhao, L. Wang, S. Zhao, X. H. Wang and S. T. Wang, *Fuel*, 2011, **90**, 2289-2293.
28 K.-I. Shimizu, H. Furukawa, N. Kobayashi, Y. Itaya and A. Satsuma, *Green Chem.*, 2009, **11**, 1627-1632.
29 J. Tian, J. H. Wang, S. Zhao, C. Y. Jiang, X. Zhang and X. H. Wang, *Cellulose*, 2010, **17**, 587-594.
30 W. P. Deng, Q. H. Zhang and Y. Wang, *Dalton Trans.*, 2012, **41**, 9817-9831.
31 F. Cavani, *Catal. Today*, 1998, **41**, 73-86.
32 I. V. Kozhevnikov, *Chem. Rev.*, 1998, **98**, 171-198.
33 N. Mizuno and M. Misono, *Chem. Rev.*, 1998, **98**, 199-217.
34 A. Onda, T. Ochi and K. Yanagisawa, *Catal. Commun.*, 2011, **12**, 421-425.
35 J. Z. Zhang, X. Liu, M. N. Hedhili, Y. H. Zhu and Y. Han, *Chemcatchem*, 2011, **3**, 1294-1298.
36 D. L. An, A. H. Ye, W. P. Deng, Q. H. Zhang and Y. Wang, *Chem. Eur. J.*, 2012, **18**, 2938-2947.
37 R. A. Assary, P. C. Redfern, J. Greeley and L. A. Curtiss, *J. Phys. Chem. B*, 2011, **115**, 4341-4349.
38 M. J. Frisch, G. W. Trucks, H. B. Schlegel, G. E. Scuseria, M. A. Robb, J. R. Cheeseman, G. Scalmani, V. Barone, B. Mennucci, G. A. Petersson, H. Nakatsuji, M. Caricato, X. Li, H. P. Hratchian, A. F. Izmaylov, J. Bloino, G. Zheng, J. L. Sonnenberg, M. Hada, M. Ehara, K. Toyota, R. Fukuda, J. Hasegawa, M. Ishida, T. Nakajima, Y. Honda, O. Kitao, H. Nakai, T. Vreven, J. A. Montgomery Jr, J. E. Peralta, F. Ogliaro, M. Bearpark, J. J. Heyd, E. Brothers, K. N. Kudin, V. N. Staroverov, T. Keith, R. Kobayashi, J. Normand, K. Raghavachari, A. Rendell, J. C. Burant, S. S. Iyengar, J. Tomasi, M. Cossi, N. Rega, J. M. Millam, M. Klene, J. E. Knox, J. B. Cross, V. Bakken, C. Adamo, J. Jaramillo, R. Gomperts, R. E. Stratmann, O. Yazyev, A. J. Austin, R. Cammi, C. Pomelli, J. W. Ochterski, R. L. Martin, K. Morokuma, V. G. Zakrzewski, G. A. Voth, P. Salvador, J. J. Dannenberg, S. Dapprich, A. D. Daniels, O. Farkas, J. B. Foresman, J. V. Ortiz, J. Cioslowski and D. J. Fox, *GAUSSIAN 09 (Revision C.01), Gaussian Inc., Wallingford, CT* 2010.
39 Y. Zhao and D. G. Truhlar, *Theor. Chem. Acc.*, 2008, **120**, 215-241.
40 R. Ditchfield, W. J. Hehre and J. A. Pople, *J. Chem. Phys.*, 1971, **54**, 724-728.
41 W. J. Hehre, R. Ditchfield and J. A. Pople, *J. Chem. Phys.*, 1972, **56**, 2257-2261.
42 Pc. Harihara and J. A. Pople, *Theor. Chem. Acc.*, 1973, **28**, 213-222.
43 P. J. Hay and W. R. Wadt, *J. Chem. Phys.*, 1985, **82**, 270-283.
44 A. Klamt and G. Schuurmann, *J. Chem. Soc.-Perkin Trans.*, 1993, **5**, 799-805.
45 A. Klamt and F. Eckert, *Fluid Phase Equilib.*, 2000, **172**, 43-72.
46 R. Seeger and J. A. Pople, *J. Chem. Phys.*, 1977, **66**, 3045-3050.
47 R. Bauernschmitt and R. Ahlrichs, *J. Chem. Phys.*, 1996, **104**, 9047-9052.
48 C. Gonzalez and H. B. Schlegel, *J. Chem. Phys.*, 1989, **90**, 2154-2161.
49 C. Gonzalez and H. B. Schlegel, *J. Chem. Phys.*, 1990, **94**, 5523-5527.
50 A. E. Reed, R. B. Weinstock and F. Weinhold, *J. Chem. Phys.*, 1985, **83**, 735-746.
51 A. E. Reed, L. A. Curtiss and F. Weinhold, *Chem. Rev.*, 1988, **88**, 899-926.
52 T. Lu and F. W. Chen, *J. Comput. Chem.*, 2012, **33**, 580-592.
53 T. Lu and F. W. Chen, *J. Mol. Graph. Model.*, 2012, **38**, 314-323.
54 T. Lu and F. W. Chen, *Acta. Chimica. Sinica.*, 2011, **69**, 2393-2406.
55 H. Eyring, *J. Chem. Phys.*, 1935, **3**, 107-115.
56 E. Wigner, *J. Chem. Phys.*, 1937, **5**, 720-723.
57 S. Kozuch and S. Shaik, *J. Am. Chem. Soc.*, 2006, **128**, 3355-3365.
58 S. Kozuch and S. Shaik, *J. Phys. Chem. A*, 2008, **112**, 6032-6041.
59 A. Uhe, S. Kozuch and S. Shaik, *J. Comput. Chem.*, 2011, **32**, 978-985.
60 C. Amatore and A. Jutand, *J. Organomet. Chem.*, 1999, **576**, 254-278.
61 R. Strandberg, *Acta. Chem. Scand.*, 1975, **29**, 359-364.
62 C. J. Dillon, J. H. Holles, R. J. Davis, J. A. Labinger and M. E. Davis, *J. Catal.*, 2003, **218**, 54-66.
63 G. A. Tsigdinos, *Ind. Eng. Chem. Prod. Res. Develop.*, 1974, **13**, 267-274.
64 V. S. Bernales, A. V. Marenich, R. Contreras, C. J. Cramer and D. G. Truhar, *J. Phys. Chem. B*, 2012, **116**, 9122-9129.
65 N. D. Feng, A. M. Zheng, S. J. Huang, H. L. Zhang, N. Y. Yu, C. Y. Yang, S. B. Liu and F. Deng, *J. Phys. Chem. C*, 2010, **114**, 15464-15472.
66 S. Bogatko, J. Moens and P. Geerlings, *J. Phys. Chem. A*, 2010, **114**, 7791-7799.
67 S. Bogatko, E. Cauet and P. Geerlings, *J. Phys. Chem. C*, 2011, **115**, 6910-6921.
68 S. Bogatko and P. Geerlings, *Phys. Chem. Chem. Phys*, 2012, **14**, 8058-8066.
69 R. Schenkel, A. Jentys, S. F. Parker and J. A. Lercher, *J. Phys. Chem. B*, 2004, **108**, 7902-7910.

70 G. N. Vayssilov, J. A. Lercher and N. Rosch, *J. Phys. Chem. B*, 2000, **104**, 8614-8623.
71 D. H. Olson, W. O. Haag and W. S. Borghard, *Micro. Meso. Mat.*, 2000, **35-36**, 435-446.

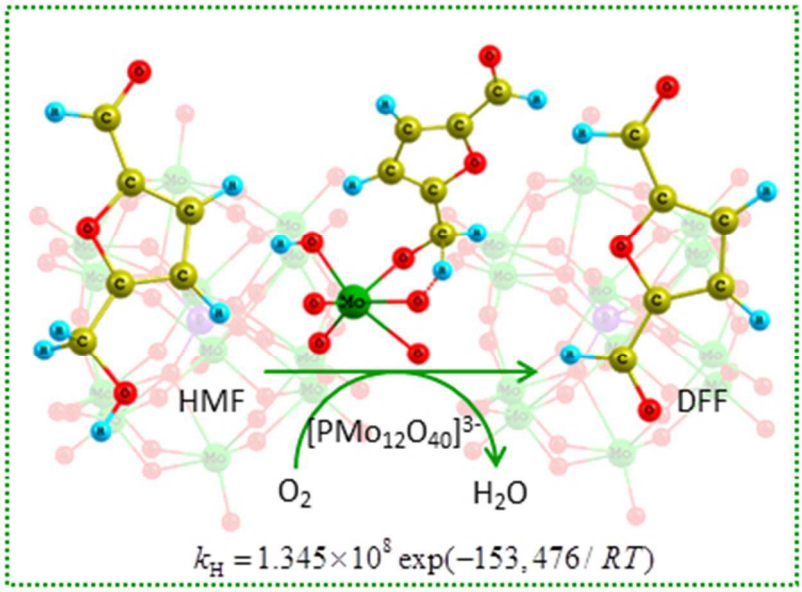

106x80mm (96 x 96 DPI)